



HAL
open science

Laser induced plasma characterization in direct and water confined regimes: new advances in experimental studies and numerical modelling

Marine Scius-Bertrand, Laurent Videau, Alexandre Rondepierre, Emilien Lescoute, Yann Rouchausse, Jan Kaufman, Danijela Rostohar, Jan Brajer, Laurent Berthe

► To cite this version:

Marine Scius-Bertrand, Laurent Videau, Alexandre Rondepierre, Emilien Lescoute, Yann Rouchausse, et al.. Laser induced plasma characterization in direct and water confined regimes: new advances in experimental studies and numerical modelling. *Journal of Physics D: Applied Physics*, 2021, 54 (5), pp.1-14. 10.1088/1361-6463/abc040 . hal-03164824

HAL Id: hal-03164824



<https://hal.science/hal-03164824v1>

Submitted on 10 Mar 2021

HAL is a multi-disciplinary open access archive for the deposit and dissemination of scientific research documents, whether they are published or not. The documents may come from teaching and research institutions in France or abroad, or from public or private research centers.

L'archive ouverte pluridisciplinaire **HAL**, est destinée au dépôt et à la diffusion de documents scientifiques de niveau recherche, publiés ou non, émanant des établissements d'enseignement et de recherche français ou étrangers, des laboratoires publics ou privés.

Laser induced plasma characterization in direct and water confined regimes: new advances in experimental studies and numerical modelling

Marine Scius-Bertrand^{1,2} , Laurent Videau^{1,3}, Alexandre Rondepierre^{2,4},
Emilien Lescoute^{1,3}, Yann Rouchausse², Jan Kaufman⁵, Danijela Rostohar⁵, Jan Brajer⁵
and Laurent Berthe² 

¹ CEA, DAM, DIF, 91297 Arpajon, France

² Arts et Métiers Institute of Technology, CNRS, CNAM, PIMM, HESAM Université, Paris 75013, France

³ CEA, Laboratoire Matière sous Conditions Extrêmes, Université Paris-Saclay, Bruyères-le-Châtel 91680, France

⁴ THALES LAS France, 78990 Elancourt, France

⁵ HiLASE Centre, Institute of Physics of the Czech Academy of Sciences, Za Radnici 828 252 41 Dolni Brezany, Czech Republic

E-mail: marine.sciusbertrand@cea.fr and laurent.berthe@ensam.eu

Abstract

Optimization of the laser shock peening (LSP) and LASer Adhesion Test (LASAT) processes requires control of the laser-induced target's loading. Improvements to optical and laser technologies allow plasma characterization to be performed with greater precision than 20 years ago. Consequently, the processes involved during laser–matter interactions can be better understood. For the purposes of this paper, a self-consistent model of plasma pressure versus time is required. The current approach is called the inverse method, since it is adjusted until the simulated free surface velocity (FSV) corresponds to the experimental velocity. Thus, it is not possible to predict the behavior of the target under shock without having done the experiments. For the first time, experimental data collected in different labs with the most up-to-date laser parameters are used to validate a self-consistent model for temporal pressure-profile calculation. In addition, the parameters characterizing the plasma (temperature, thickness and duration) are obtained from the ESTHER numerical code, together with the amount of ablated matter. Finally, analytic fits are presented that can reproduce any pressure–temporal profiles in the following domains of validity: intensities, I , ranging from 10 to 500 GW cm⁻² and pulse durations, T_{pul} , between 5 and 40 ns for the direct-illumination regime at 1053 nm, I ranging from 1 to 6 GW cm⁻² and T_{pul} between 10 to 40 ns in the water-confined regime at 1053 nm, and I from 1 to 10 GW cm⁻² and T_{pul} between 7 and 20 ns in the water-confined regime at 532 nm. These temporal pressure profiles can then be used to predict the aluminum target's behavior under laser shock using mechanical simulation software.

Keywords: laser shock, LSP, LASAT, laser-matter interaction, WCR, VISAR, plasma

Abbreviations:

CCD	charge-coupled device
DOE	diffractive optical elements
FWHM	full width at half-maximum
FSV	free surface velocity
GCLT	transportable laser shock generator
LASAT	LASer Adhesion Test
LSP	laser shock peening
SCG	Steinberg-Cochran-Guinan
VISAR	velocity interferometer system for any reflector
WCR	water-confined regime

1. Introduction

Laser shock is used in several processes such as the laser shock peening (LSP) and the LASer Adhesion Test (LASAT). The propagation of shock and release waves through materials induces compression and traction zones [1, 2]. While the residual stresses arising from the compression of matter are relevant for the LSP treatment [3], the LASAT process exploits the traction peak stress that arises at the meeting point of two release waves [4, 5]. The LSP treatment, when applied to a metallic target, has already proven its capability to improve mechanical properties and fatigue performance [6–10]: crack initiation is inhibited and crack growth is delayed. The LASAT capability was first demonstrated by Vossen [11]; its state of the art was published in 2011 [12]. Several studies since have shown that it can be used as an extended non-destructive test for aeronautical bonding [13–15].

The application of a high-powered laser to a metallic surface causes vaporization of a layer a few micrometers thick, leading to the formation of an expanding plasma [16, 17]. In reaction to the plasma expansion, a mechanical loading, equivalent to an ablation pressure (P_{abl}), is applied to the target, resulting in a shock wave that propagates through the material (figure 1). The illumination of the surface can be direct (figure 1(b)) or in a confined regime (figure 1(a)). The confinement can be any medium transparent to the laser wavelength that will slow the expansion of the plasma. The use of confinement therefore increases the equivalent pressure by up to one order of magnitude and makes the shock wave last two to three times longer than the pulse duration [18–21]. However, in a dielectric medium such as water or air, a breakdown phenomenon can occur at certain laser intensities, leading to a pressure saturation and a shorter shock wave duration [22–25]. The determination of the intensity threshold above which breakdown appears is essential to identify the usable range of pressures as a function of incident power density.

LSP and LASAT technologies use similar lasers, neodymium-doped yttrium aluminum garnet (Nd:YAG) or neodymium-doped glass (Nd:glass), with wavelengths ranging from 532 to 1064 nm and energies from a few joules

to several tens of joules focused on millimeter-sized focal spots. It is essential to master the laser-induced plasma in order to control the process. In addition, this investigation offers the opportunity to examine material properties under shock. Currently, some models already exist that can characterize the physical processes of a confined laser shock [21] or calculate the maximal induced pressure from the experimental velocities [26]. However, their validation has been done using one set of laser parameters, with different means of pressure characterization but with a lack of laser metrology and no reliable beam-quality [21–23, 27]. In addition, there is no self-consistent model for the prediction of plasma temporal pressure profiles. The improvement of experimental and numerical tools over the past few years has enabled new advances in plasma characterization aiming at verifying recent experimental reliability as well as extracting a self-consistent numerical model. Therefore, for the first time, this work consists of a collection of an extensive range of experiments to validate a model able to predict the loading profile necessary to simulate the laser shock process. Based on the ESTHER numerical code, it permits a characterization of the plasma (temperature, duration and thickness). This paper presents an experimental and numerical study of laser–matter interaction in the water-confined regime and direct illumination at three laser facilities allowing different focal spots (round and square) and variable pulse shapes and durations. For every experiment, an effort has been made to characterize the laser in terms of its beam profile, energy and temporal pulse shape. First, we present velocity interferometer system for any reflector (VISAR) measurements of free surface velocity (FSV) versus time for pure aluminum. These are then compared to the numerical simulation obtained from the ESTHER code. Thanks to its laser–matter interaction prediction module, the plasma temperature is obtained from the code as well as the equivalent ablation pressure and the amount of ablated materials. Finally, practical scaling laws are extracted from these results. The latter provide a plasma temporal pressure profile for any of the above configurations, which can be used to simulate the behaviour of aluminum under laser shock using mechanical simulation software.

2. Experimental study

Three laser facilities with several setups were used: Héphaïstos in the Process and Engineering in Mechanics and Materials laboratory (PIMM lab) (Paris), the HiLASE research center (Prague) and the Transportable Laser Shock Generator (GCLT) of the French Alternative Energies and Atomic Energy Commission (CEA/DAM/DIF) (Paris). Each source is described more precisely thereafter. A 2–3 mm water-confined regime was used consistently at all experimental facilities (figure 1(a)), achieved by depositing water on the

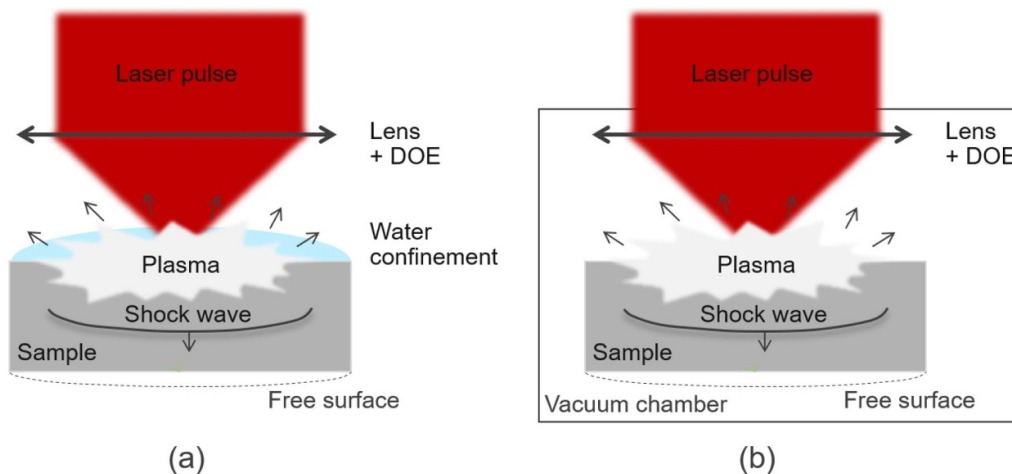


Figure 1. A schematic view of the experimental setups (a) in water-confined regime performed at Héphaïstos, HiLASE and GCLT, (b) in direct-interaction regime performed at GCLT.

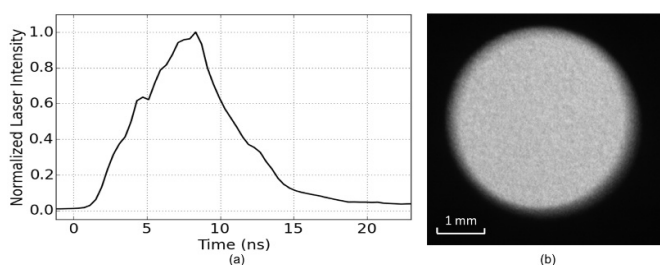


Figure 2. (a) Temporal pulse of 7 ns at Hephaisstos. (b) Typical CCD image of a $\phi = 4$ mm round top-hat focal spot.

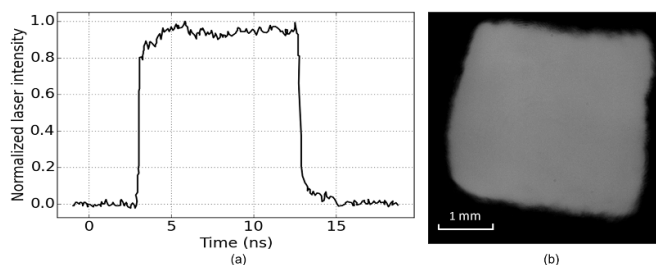


Figure 3. (a) Top-hat temporal profile of a 10 ns pulse at HiLASE. (b) Spatial shape profile for a $\phi = 3.5$ mm square top-hat laser spot.

sample's surface. In addition, the vacuum chamber of the GCLT (figure 1(b)) was used for direct irradiation regime. A particular effort was made to ensure precise knowledge of the experimental parameters. The target laser energies are measured and saved for each shot using calibrated calorimeters. Diffractive optical elements (DOE) were added to every beam path at Héphaïstos and GCLT to homogenize their spatial distributions [14]. Before starting the experiments, the on-target focal spot diameters (ϕ) are measured using a charge-coupled device (CCD) camera and the temporal profiles are measured using photodiodes. The GCLT can change these profiles on demand, therefore they are measured and saved for each shot. The rear FSVs were measured using VISAR [26, 28–30]. A 100 μm -diameter laser probe is focused on the back face of the sample and aligned to scan the middle of the working laser's focal spot. The photomultiplier's response time offers time-resolved velocity measurements with a precision on the nano-second scale. The global uncertainty of the velocity measurement and the corresponding laser intensity is estimated to be $\pm 15\%$ rms.

2.1. Laser facilities

The Héphaïstos platform uses a Thales Gaïa High Power laser composed of two Nd:YAG lasers at 532 nm. Together, they can deliver up to 14 J with a pulse duration of 7 ns full width

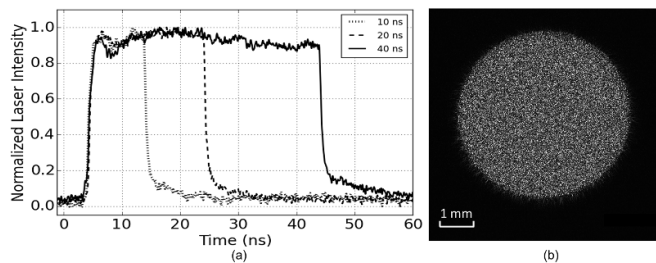


Figure 4. (a) Top-hat temporal profile obtained for 10, 20 and 40 ns requests at GCLT. (b) Typical CCD image of a $\phi = 5.1$ mm round top-hat focal spot.

at half maximum (FWHM) of a Gaussian pulse (figure 2(a)). The focal spot diameters are 3 and 4 mm, leading to intensities ranging from 0.7 to 13 GW cm^{-2} . The spatial shape of a 4 mm focal spot taken by a CCD camera is displayed in figure 2(b).

The main laser system of the HiLASE research center is called BIVOL. It is a diode-pumped solid-state laser working at 1029 nm and delivering 10 ns pulses with energy levels of up to 105 J [31]. Both the spatial and temporal shapes of the pulses are square (figure 3). The use of a 3.5 mm focal spot led to intensities ranging from 0.6 to 11.8 GW cm^{-2} .

The GCLT is based on an Nd:glass laser (Lumibird) with a wavelength of 1053 nm that delivers pulses from 4 to 100 ns

Table 1. Parameters used for the Steinberg–Cochran–Guinan (SCG) material model [34] with an aluminum target (99.999%, laminated).

Material	Y_0 (MPa)	Y_{\max} (MPa)	β	n	ε_i	G_0 (GPa)	G'_p	G'_T (GPa/K)
Aluminum	120	160	4000	0.27	0	27.1	1.8	-1.7×10^{-2}

with energies of up to 40 J. The laser pulse temporal profile can be chosen to be, for example, Gaussian-like, triangular or top hat. Figure 4(a) displays the top-hat pulse duration obtained for a requested pulse of 10–40 ns. A vacuum chamber enables the study of the direct-illumination regime. For the water-confined regime, a 5.1 mm focal spot was used (figure 4(b)), leading to intensities ranging from 0.2 to 11.5 GW cm⁻². In order to reach the same induced pressure in the direct-irradiation regime, the intensities have to be much higher (from 8 to 200 GW cm⁻²). With the same laser energies available, the laser focal spots were 2.5 and 1 mm.

2.2. Materials

The thicknesses of the samples were chosen in accordance with the focal spots to avoid edge effects by making the ratio of sample thickness to focal spot diameter smaller than 0.25 [32, 33]. This study was thus conducted using two thicknesses (100 μm and 500 μm , respectively, for direct illumination and the water-confined regime) of pure aluminum. The Steinberg–Cochran–Guinan (SCG) model was used to obtain their elastoplastic behaviors (cf section 3) [34]. The mechanical properties used in this study are displayed in table 1 [35]. The initial and maximal yield strengths are Y_0 and Y_{\max} , respectively (in the von Mises sense), β and n are work-hardening parameters, ε_i is the initial equivalent plastic strain, G_0 is the shear modulus at the reference state (temperature $T = 300$ K, pressure $P = 0$ and $\varepsilon = 0$), and G'_p and G'_T are the shear modulus derivatives with respect to the pressure and temperature, respectively.

2.3. Experimental Results

This section presents VISAR measurements performed under two illumination regimes at three laser facilities (Hephaistos, HiLASE and GCLT). For each configuration, the dependences of the rear FSV measurements on the laser pulse duration ΔT (ns) and/or the intensity I (GW cm⁻²) are presented (figures 5 and 7) together with the simulations, which will be discussed in section 3. Plotting the maximal FSV versus the laser intensity (figures 6 and 8) enables us to observe the global behavior of the target under direct and water-confined irradiation, to identify the breakdown phenomenon threshold, and to compare the results from one installation to another.

2.3.1. Direct illumination regime. This study is based on a large set of data gathered from numerous experiments carried out with several focal spots, laser intensities, and pulse durations, ensuring a wide range of results. Some representative signals of the FSV as a function of time are displayed in figure 5 for $\Delta T = 10, 20$ and 40 ns at different power densities. A comparison with the simulation (colored dashed lines)

and the $\pm 15\%$ uncertainty of the incident power density (grey area) will be discussed in section 3. The first peak is of particular interest, since it corresponds to the first emergence of the shock wave and has a direct relationship to the plasma pressure [23, 26]. The other peaks correspond to wave reflections within the target. By comparing the first maxima for two pulse durations (10 and 20 ns, figure 5(a) 1 and 5(b) 1) it is possible to conclude that pulse duration does not affect the respective velocity maxima (115 m s⁻¹ for $I = 16.7$ GW cm⁻² and 60 m s⁻¹ for $I = 8.1$ GW cm⁻²): the maximum velocity is only influenced by applied peak intensities. The peak width is related to the pulse duration: a longer pulse duration (from 10 to 20 ns) induces broader peaks (from 16 to 28 ns at half maximum). In the case of a 40 ns pulse striking a 100 μm sample, the shock duration is longer than the time needed by the wave to go back and forth in the target (37 ns), hence the release wave arriving at the end of the laser pulse reloads the reflected release wave and the peak increases again before decreasing to its minimum (figure 5(c)).

The first peak maximum of the rear FSV was determined for three pulse durations (10, 20 and 40 ns) and two focal spot sizes (1.1 and 2.5 mm). In the case of a clear peak (figures 5(a) and (c)), its highest value was extracted, otherwise the maximum was set to the mean value of the plateau (figure 5(b)). Figure 6 collates the maximum velocities of the first peaks extracted from the measurements for all pulse durations and spot diameters included in the direct illumination regime. From this graph, it is clear that neither the focal spot nor the laser pulse duration has an influence on the maximal FSV in the direct irradiation regime when applied to a 100 μm pure-aluminum target. The maximal FSV increases with the intensity in the entire range studied (from 8 to 195 GW cm⁻² corresponding, respectively, to velocities of 50 and 630 m s⁻¹).

2.3.2. Water confined regime (WCR). Water confined regime experiments were carried out at three wavelengths (532, 1029 and 1053 nm) with four pulse durations (7, 10, 20 and 40 ns) and four focal spots (3, 3.5, 4 and 5 mm). Typical velocity profiles are displayed in figure 7. First of all, the effect of confinement on the pressure should be noted; less intensity is needed to reach the same velocities in the water-confined regime (WCR) than with the direct-irradiation regime. For example, in the direct illumination regime, a top-hat pulse of 10 ns from the GCLT platform with 112 GW cm⁻² induces a rear FSV of almost 400 m s⁻¹, whereas only 5 GW cm⁻² at the same pulse duration is required in the WCR for almost the same FSV. This is in good agreement with a previous study showing that the use of confinement increases the ablation pressure [21]. Figure 7 displays the FSV versus time for (a) 7 ns Gaussian pulses at 532 nm and (b) 10 ns top-hat pulses at

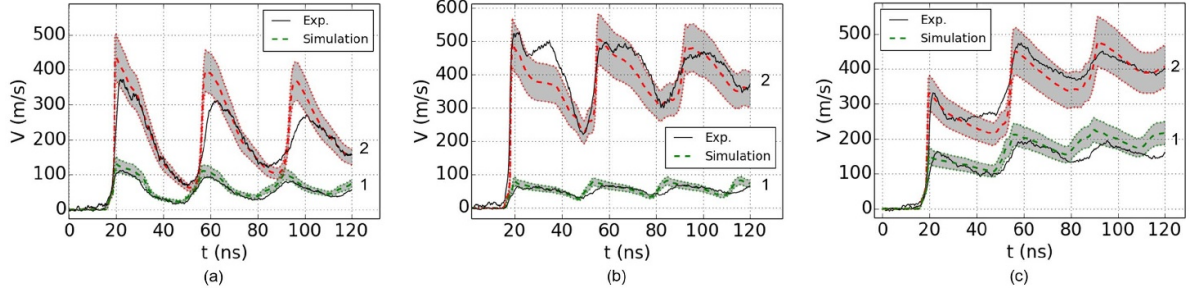


Figure 5. A comparison of the simulated (colored dashed lines) and experimental (black lines) results for 99.999% pure aluminum, thickness = 100 μm , GCLT, 1053 nm, direct illumination, $\phi = 1.1$ mm: (a) $\Delta T = 10$ ns, (1) $I = 16.7$ GW cm^{-2} , (2) $I = 112.0$ GW cm^{-2} , (b) $\Delta T = 20$ ns, (1) $I = 8.1$ GW cm^{-2} , (2) $I = 133.6$ GW cm^{-2} , (c) $\Delta T = 40$ ns, (1) $I = 24.7$ GW cm^{-2} , (2) $I = 71.1$ GW cm^{-2} . Uncertainty of the simulation $\varepsilon = 15\%$ (grey area).

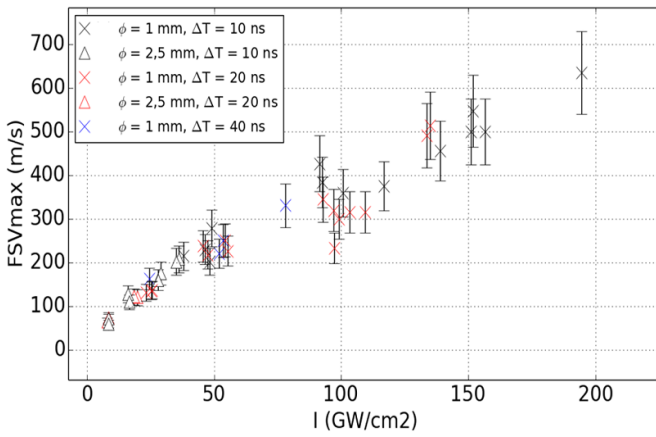


Figure 6. FSV_{max} versus laser intensity I . 99.999% pure aluminum, thickness = 100 μm , GCLT—1053 nm, direct illumination, $\phi = 1.1$ and 2.5 mm, $\Delta T = 10$ ns, 20 ns and 40 ns.

1053 nm. In this case, the shape of the FSV peaks is not influenced by the laser-pulse shape nor the wavelength: the peaks widths durations at half maximum are 32 and 20 ns, respectively. When using longer top-hat pulse durations, the widths of the peaks increase: pulses of 20 and 40 ns (figures 7(c) and (d)) result in FSV first peak widths at half maximum of 41 and 79 ns, respectively.

The maximal rear FSV was set the same as for the direct illumination regime, and is plotted versus the laser intensity in figure 8. From these graphs, the influence of the wavelength and the pulse duration on the FSV maxima is established. However, small variations of the wavelength (from 1029 to 1053 nm) and focal spots (round and square) do not affect the maximum peak velocity. The results of the experiments carried out at the two laser facilities (GCLT and HiLASE) are consistent with each other (figure 8(b)), demonstrating the reliability of the method. For all sets of data obtained, two different behaviors can be observed: firstly, the velocities increase as a function of power density; secondly, the maximal velocities saturate from a threshold corresponding to the intensity (I_{th}), above which the plasma breakdown has a detrimental effect on the maximal FSV. For the 7 ns laser pulse at 532 nm, the I_{th} is equal to 8–10 GW cm^{-2} with a maximal FSV of 720 m s^{-1}

(figure 8(a)). For laser pulses at 1029 and 1053 nm with pulse durations of 10, 20 and 40 ns, the I_{th} values are equal to 5 to 6, 3 to 4 and 2 to 3 GW cm^{-2} , respectively, with maximal velocities of 530, 440 and 300 m s^{-1} (figures 8(b)–(d)). These thresholds are collated in table 2.

3. Numerical study

The numerical study was performed using one-dimensional Lagrangian code called ESTHER. It is widely described in the literature [13, 35–37]. In the studied range of power densities, the plasma is dominated by inverse bremsstrahlung laser absorption and hydrodynamic phenomena including ionization, phase transformation, temperature and pressure determination. In the code, the material stack is divided into several cells. The laser–matter interaction is reproduced by solving the Helmholtz equations within each cell using the complex refractive indexes given by Palik’s tables [38] for the solid state, and calculated from the Lorentz plasma model [39] in the plasma state. The hydrodynamics of each cell are modelled by solving equations for the cell position’s evolution together with the equations for the conservation of mass, momentum and energy in finite volumes in the planar mono-dimensional hypothesis. The global hydrodynamic in the entire stack of cells is described using, in our case, a SESAME-tabulated state equation provided by the Los Alamos National Laboratory. The mechanical behavior of the stack is simulated using the SCG model [34]. The code reliability in the direct-irradiation regime at 1053 nm and the WCR at 532 nm was proven by Bardy [35]. The aim of this study is to extend its range of application under WCR at 1053 nm to extract ablation pressure temporal profiles and find numerical equations to reproduce them without a laser–matter interaction code. In addition, plasma temperature profiles and the ablated layer thickness are obtained from the simulation to evaluate the impact of the plasma laser on the surface of the material. The SESAME equation for state number 3720 and the aluminum elastoplastic model properties are taken directly from previous studies (cf table 1) [35]. For the WCR, all the parameters from the previous study were adopted, except for the optical constant of water, which had been adapted for the 1053 nm wavelength

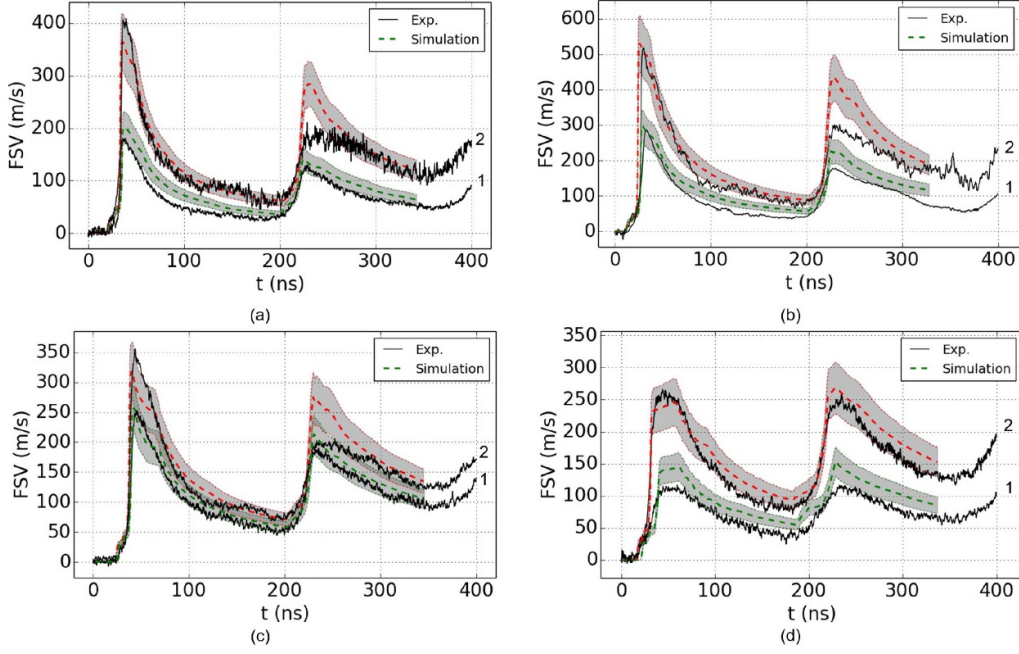


Figure 7. A comparison of the simulated (colored dashed lines) and experimental (black lines) results for pure aluminum, thickness = $500 \mu\text{m}$, WCR. (a) Hephaïstos, 532 nm, $\Delta T = 7 \text{ ns}$, $\phi = 4 \text{ mm}$, (1) $I = 2.4 \text{ GW cm}^{-2}$, (2) $I = 5.9 \text{ GW cm}^{-2}$, (b) GCLT, 1053 nm, $\Delta T = 10 \text{ ns}$, $\phi = 5 \text{ mm}$, (1) $I = 2.3 \text{ GW cm}^{-2}$, (2) $I = 5.0 \text{ GW cm}^{-2}$, (c) GCLT, 1053 nm, $\Delta T = 20 \text{ ns}$, $\phi = 5 \text{ mm}$, (1) $I = 1.4 \text{ GW cm}^{-2}$, (2) $I = 2.3 \text{ GW cm}^{-2}$, (d) GCLT, 1053 nm, $\Delta T = 40 \text{ ns}$, $\phi = 5 \text{ mm}$, (1) $I = 0.4 \text{ GW cm}^{-2}$, (2) $I = 1.1 \text{ GW cm}^{-2}$. Uncertainty of the simulation $\varepsilon = 15 \%$ (grey area).

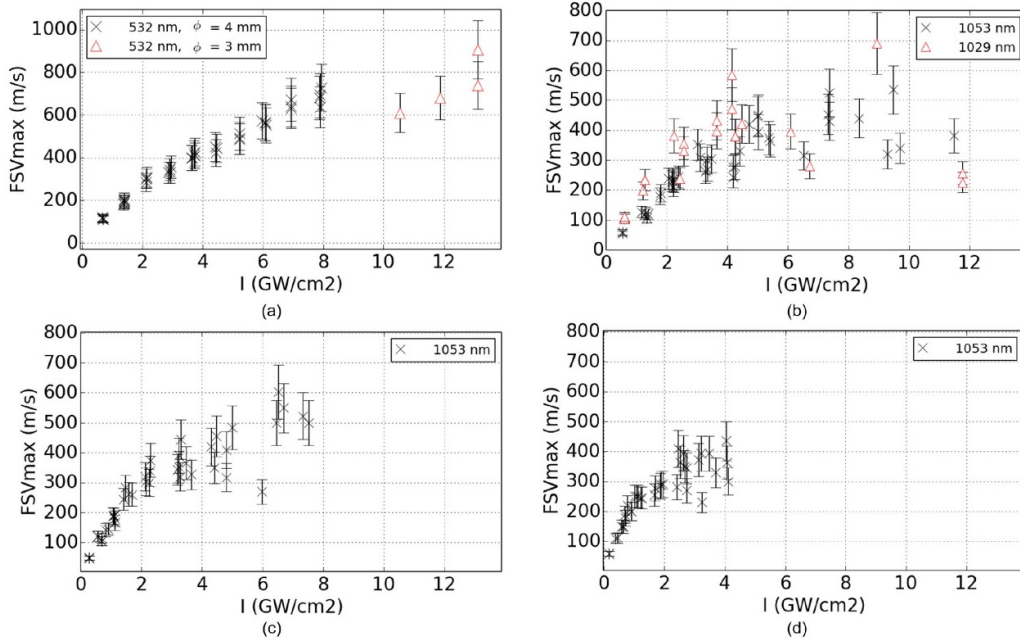


Figure 8. FSV_{max} versus laser intensity I . Pure aluminum, thickness = $500 \mu\text{m}$, WCR: (a) Hephaïstos, 532 nm, $\phi = 3$ and 4 mm , $\Delta T = 7 \text{ ns}$; (b) GCLT: 1053 nm; HiLASE: 1029 nm; $\phi = 5$ and 3.5 mm , $\Delta T = 10 \text{ ns}$; (c) GCLT, 1053 nm, $\phi = 5 \text{ mm}$, $\Delta T = 20 \text{ ns}$; (d) GCLT, 1053 nm, $\phi = 5 \text{ mm}$, $\Delta T = 40 \text{ ns}$.

($n_1 = 1.33$, $n_2 = 1.3 \times 10^{-6}$) [40] where $n_1 + n_2$ is the complex refractive index.

3.1. Free surface velocity

The simulations of the FSV under direct illumination and the WCR are displayed in figures 5 and 7 (colored dashed lines)

and compared with the experimental results (black lines). The simulation uncertainty is directly linked to the intensity input deduced from the focal spot and energy experimental measurements (cf section 2). Therefore it is also taken at $\pm 15\%$. It is represented by grey areas. The SCG mechanical model is correct for every configuration and its good agreement with the experiments is shown in figures 5 and 7.

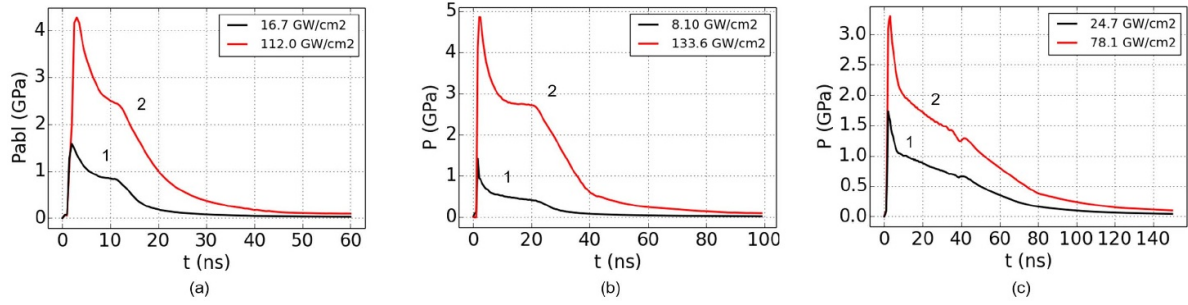


Figure 9. P_{abl} versus time. 99.999% pure aluminum, thickness = 100 μm , GCLT, 1053 nm, direct illumination, $\phi = 1.1$ mm: (a) $\Delta T = 10$ ns, (1) $I = 16.7$ GW cm^{-2} , (2) $I = 112.0$ GW cm^{-2} ; (b) $\Delta T = 20$ ns, (1) $I = 8.1$ GW cm^{-2} , (2) $I = 133.6$ GW cm^{-2} ; (c) $\Delta T = 40$ ns, (1) $I = 24.7$ GW cm^{-2} , (2) $I = 78.1$ GW cm^{-2} .

In both illumination regimes, the first peak amplitude is accurately determined when ε is taken in account. In the direct-illumination regime, small discrepancies in the peak shape and duration can be seen (figures 5(a) 2 and (b) 2), highlighting a potential area for improvement in the elastoplastic model. However, this study is focusing on the plasma pressure, which is directly related to the first peak and thus will not be affected by those discrepancies. In the direct-illumination regime as well as the WCR, the experimental curves for each wavelength and pulse duration are accurately described by the code when only the laser power density changes. This supports the validity of the code at 532 nm in the WCR with $\Delta T = 7$ ns and intensities ranging from 2.4 to 6 GW cm^{-2} and at 1053 nm, as follows:

- $\Delta T = 10$ ns, laser intensities ranging from 15 to 110 and 1.3 to 5 GW cm^{-2} for direct illumination and WCR, respectively
- $\Delta T = 20$ ns, laser intensities ranging from 10 to 130 and 1.5 to 2.3 GW cm^{-2} for direct illumination and WCR, respectively
- $\Delta T = 40$ ns, laser intensities ranging from 25 to 80 and 0.8 to 2 GW cm^{-2} for direct illumination and WCR, respectively.

Consequently, the interesting physical data, such as the pressure as a function of time, can be extracted from the code for each corresponding validity domain.

3.2. Ablation pressure

The ablation pressure, P_{abl} , versus time was obtained from the code at the ablation front location. Figure 9 presents the results for the ablation pressures at 10, 20 and 40 ns at 1053 nm in the direct-illumination regime. These correspond to the conditions presented in figure 5. The pulse duration has a strong influence on the shape of the pressure temporal profile. First, the pressure rises drastically when the plasma is heated by the laser, then a plateau can be observed until the end of the laser pulse. Finally, when the laser pulse ends, the pressure drops dramatically until the ambient pressure is reached, following adiabatic matter expansion.

In the WCR, the same method was applied to obtain the pressure from the simulation of the FSV presented in figure 7. In the case of a 7 ns Gaussian pulse at 532 nm (figure 10(a)) the pressure profile increases slowly during the few ns needed to warm up the matter and create the plasma. Then it increases almost as a Gaussian up to the maximal ablation pressure ($P_{abl,max}$); finally it reduces as the matter expands. For pressure profiles extracted at 1053 nm, the three steps identified in the direct-illumination regime are also visible in the WCR. However for the 20 and 40 ns pulses (figures 10(c) and (d)), the profiles are very similar with an almost perfectly flat plateau corresponding to the pulse duration. The pulse duration does not affect the maximal value; a 2.3 GW cm^{-2} pulse with top-hat pulses of either 10 or 20 ns will induce maximal ablation pressures of 2.5 or 2.7 GPa, respectively (figures 10(b) 1 and (c) 2).

To simulate the behavior of the target under laser shock, the temporal pressure profiles extracted from ESTHER (figures 9 and 10) were used instead of the laser-matter interaction module. The resulting FSV profiles are similar to the ones presented in figures 5 and 7, confirming the reliability of the temporal pressure profiles. Thanks to the model developed within the code, it is now possible to obtain the pressure as a function of time to calculate the FSVs of all the experiments realized within the area of validity defined in section 3.1.

3.3. Plasma parameters

The plasma temperature at the end of the laser pulse has been extracted from the entire simulated stack for each laser configuration (figures 5 and 7). Figure 11 displays the plasma temperatures for different incident laser intensities (I) with (a) 10, (b) 20 (c) and 40 (d) ns laser pulse durations in the direct illumination regime. The surface of the target is defined as $x=0$. The laser is, by convention, coming from the right of the stack. The warmest region is the plasma corona with temperatures from 10 to 15 eV for any pulse duration. The shock front is propagating through the target with temperatures from 2 eV to room temperature (0.03 eV). The amount of ablated aluminum is proportional to the pulse duration and the incident laser intensity. At $\Delta T = 20$ ns, with intensities of 8.1

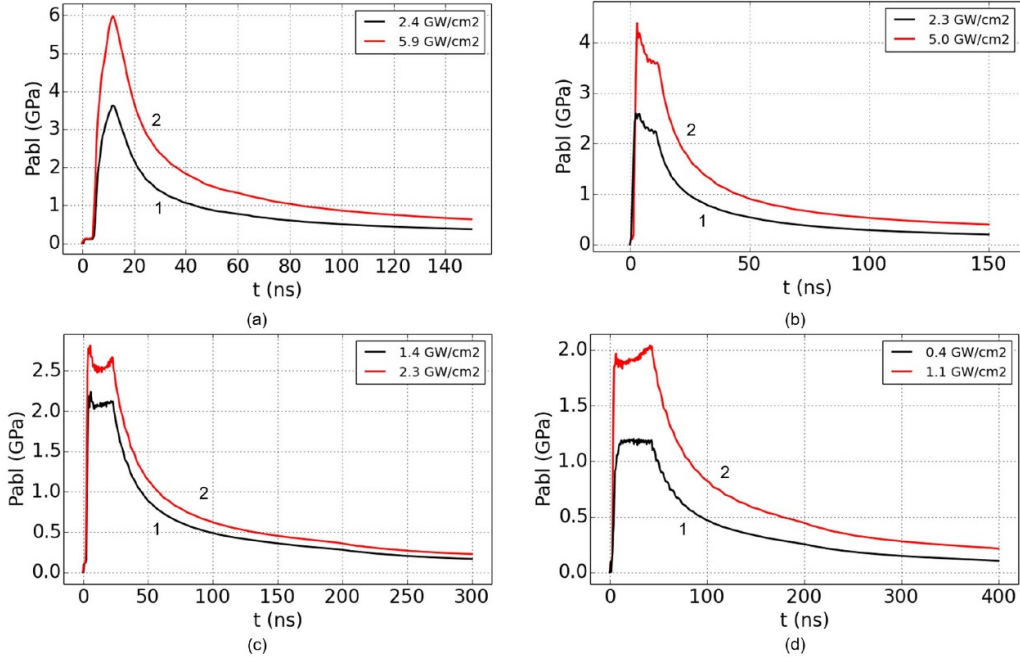


Figure 10. P_{abl} versus time. 99.999% pure aluminum, thickness = 500 μm , WCR: (a) Hephaistos, 532 nm, $\Delta T = 7$ ns, $\phi = 4$ mm, (1) $I = 2.4$ GW cm^{-2} , (2) $I = 5.9$ GW cm^{-2} ; (b) GCLT, 1053 nm, $\Delta T = 10$ ns, $\phi = 5$ mm, (1) $I = 2.3$ GW cm^{-2} , (2) $I = 5.0$ GW cm^{-2} ; (c) GCLT, 1053 nm, $\Delta T = 20$ ns, $\phi = 5$ mm, (1) $I = 1.4$ GW cm^{-2} , (2) $I = 2.3$ GW cm^{-2} , (d) GCLT, 1053 nm, $\Delta T = 40$ ns, $\phi = 5$ mm, (1) $I = 0.4$ GW cm^{-2} , (2) $I = 1.1$ GW cm^{-2} .

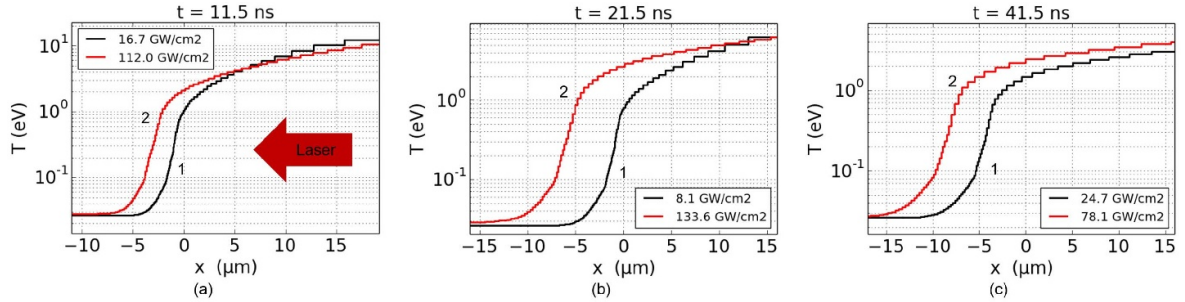


Figure 11. Temperature versus position. 99.999% Pure aluminum, thickness = 100 μm , GCLT, 1053 nm, direct illumination, $\phi = 1.1$ mm: (a) $\Delta T = 10$ ns, (1) $I = 16.7$ GW cm^{-2} , (2) $I = 112.0$ GW cm^{-2} , (b) $\Delta T = 20$ ns, (1) $I = 8.1$ GW cm^{-2} , (2) $I = 133.6$ GW cm^{-2} , (c) $\Delta T = 40$ ns, (1) $I = 24.7$ GW cm^{-2} , (2) $I = 78.1$ GW cm^{-2} .

and 133.6 GW cm^{-2} , 5 and 13 μm of aluminum are ablated, respectively.

In the WCR, the plasma temperature was extracted at the time when the pressure and the temperature were maximal, which corresponds to 12.5 ns for 7ns Gaussian pulses. In the case of 10, 20 and 40 ns top-hat pulses, the maximum temperature is at the end of the pulse duration (11.5, 22.5 and 42.5 ns precisely). The plasma temperature is displayed for laser pulses at 532 and 1053 nm in figure 12. In ESTHER, the modelling of the plasma under the WCR is composed of Al (black) and H_2O (blue) media. The temperature range is similar for all laser configurations (8–14 eV). With the wavelength and incident laser intensity kept constant, the plasma thickness, L , and temperature, T , are proportional to the pulse duration. In figure 12, the temperatures are 9 and 13 eV and the plasma lengths 9 and 20 μm , respectively, for 10 ns ((b) 1) and 20 ns ((c) 2) top-hat pulses. These results are in agreement with

Fabbro's model [21] ($L = 7$ μm for $I = 10$ GW cm^{-2} and $\Delta T = 10$ ns on a 10 mm copper target confined with glass). At the end of the laser pulse, the ablated zone can be evaluated using the temperature profile; table 2 presents these values together with the plasma thickness for every configuration. For the laser shock process, it is interesting to know the depth of the vaporized material, to quantify the required thermal protection [41, 42].

4. Scaling laws

The reliability of the numerical code and the extracted pressure profile was established in section 3. The pressure versus time relation is of particular interest, since it enables any code to calculate the behavior of materials under shock, without the need for a laser–matter interaction module. However, each

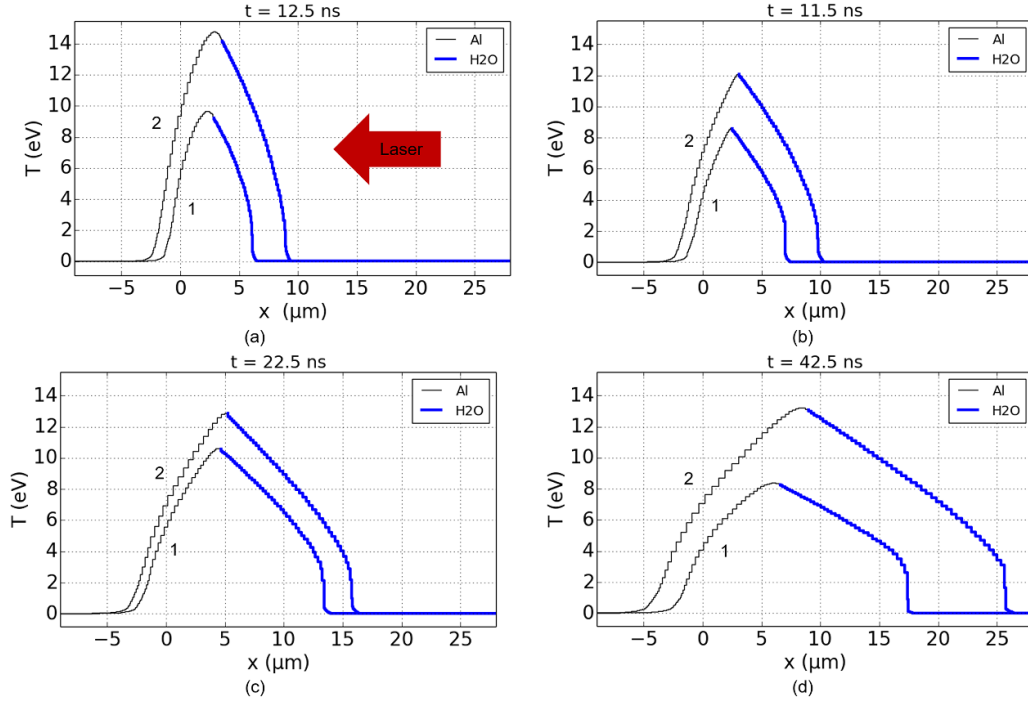


Figure 12. Temperature versus position. 99.999% pure aluminum, thickness = 500 μm , WCR (a) 532 nm, $\Delta T = 7$ ns, $\phi = 4$ mm, (1) $I = 2.4$ GW cm^{-2} , (2) $I = 5.9$ GW cm^{-2} , (b) GCLT, 1053 nm, $\Delta T = 10$ ns, $\phi = 5$ mm, (1) $I = 2.3$ GW cm^{-2} , (2) $I = 5.0$ GW cm^{-2} , (c) GCLT, 1053 nm, $\Delta T = 20$ ns, $\phi = 5$ mm, (1) $I = 1.4$ GW cm^{-2} , (2) $I = 2.3$ GW cm^{-2} , (d) GCLT, 1053 nm, $\Delta T = 40$ ns, $\phi = 5$ mm, (1) $I = 0.4$ GW cm^{-2} , (2) $I = 1.1$ GW cm^{-2} .

ablation pressure curve that is obtained requires the ESTHER code and a few minutes of calculation. The aim of this section is to present an analytic formula for the pressure dependence on the laser wavelength, pulse duration and incident intensity for the direct and water confined regimes. To support this aim, tens of simulations were run within the validity area defined by the experiments, i.e. at 532 nm in the WCR with T_{pul} between 7 and 20 ns and intensities ranging from 1 to 10 GW cm^{-2} and at 1053 nm for the WCR, T_{pul} between 10 and 40 ns and intensities I from 1 to 6 GW cm^{-2} and for direct illumination regime, T_{pul} between 5 and 40 ns and intensities I from 10 to 500 GW cm^{-2} . Numerical fits that can reproduce the temporal pressure profiles were then found. Finally, two methods yielding the maximum pressure are compared: the first is extracted from a numerical fit of the pressure temporal profile, and the second is calculated from the experimental FSVs presented in figures 5 and 7, using formula (1) [26].

$$P_{\text{max}} = \rho_0 \left(C_0 + S \frac{FSV_{\text{max}}}{2} \right) \frac{FSV_{\text{max}}}{2} + \Delta P + \frac{2}{3} \sigma_{Y_0} \quad [\text{GPa}] \quad (1)$$

where ρ_0 is the density of the material [gm^{-3}], C_0 is the sound velocity in this material [m s^{-1}], S is the parameter regulating the growth of the shock speed with the material speed, σ_{Y_0} the elastic limit [GPa], and ΔP the attenuation (hydrodynamic and elastic-plastic) [GPa]. ΔP is calculated numerically accordingly to [25]. It has to be noticed that the fit is only valid before the water breakdown power density.

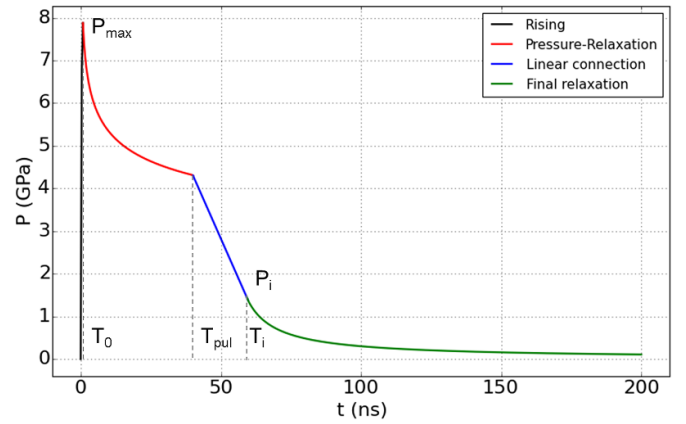


Figure 13. Analytic temporal pressure profile corresponding to a 40 ns top-hat pulse at 1053 nm with an incident laser intensity of 250 GW cm^{-2} under direct laser illumination.

4.1. Direct illumination regime

To describe the pressure temporal profile, the temporal area was divided into four zones represented in figure 13; each zone is reproduced by one fit. T_0 and T_i are set at 0.5 ns and $\frac{3}{2}T_{\text{pul}}$, respectively, for the following calculations.

- Linear rising $t \leq T_0$: $P(t) = P_{\text{max}} \left(\frac{t}{T_0} \right)$
- Pressure/relaxation zone $T_0 \leq t \leq T_{\text{pul}}$: $P(t) = P_{\text{max}} \left(\frac{T_0}{t} \right)^p$

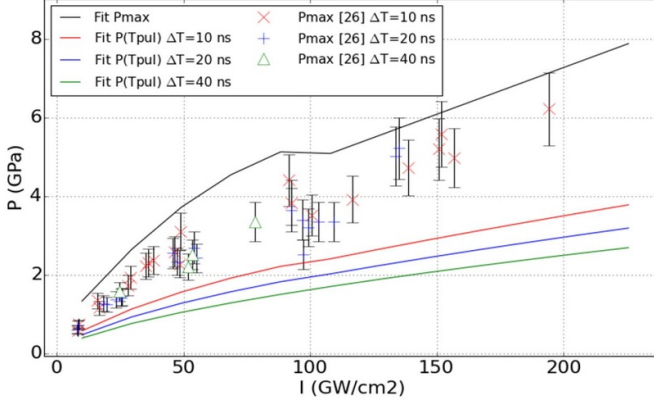


Figure 14. Maximum pressures calculated according to the analytic fit and formula (1), together with the pressure at the end of the pulse duration calculated according to the analytic fit for 10, 20 and 40 ns top-hat pulses at 1053 nm under direct illumination.

- Linear connection $T_{\text{pul}} \leq t \leq T_i$ connection between the points $[T_{\text{pul}}; P(T_{\text{pul}})]$ and $[T_i; P_i = P(T_i)]$
- Final release zone $t \geq T_i : P(t) = P_i \left(\frac{T_i - T_i \delta}{t - T_i \delta} \right)^n$.

The parameters P_{max} , P_i (pressure at time equals T_i), p , n and δ were adjusted for the entire intensity and pulse duration range. On the contrary, the parameters P_{max} and p do not depend on the pulse duration, therefore they were adjusted for the longest pulse duration, i.e 40 ns. P_m corresponds to the minimal pressure obtained at the end of this pulse duration. The three other parameters related to the relaxation, P_i , n , and δ depend on the pulse duration T_{pul} . They are all given by the equations in A.1.

The pressure profiles obtained with the above equations are in good agreement with the one obtained via the laser–matter interaction module in ESTHER. Consequently, the FSVs calculated by the code using the pressure profile and the fit are similar. Thanks to the analytically fitted curves, it is possible to reproduce the material behavior induced by laser–matter interaction using any mechanical simulation software. In the direct-illumination regime, the temporal laser pulse and pressure profile do not have the same shape, as can be seen in figure 9. There is indeed a sharp peak at the beginning of the plateau that makes it irrelevant to describe the ablation pressure using only its maximal value. As an illustration, figure 14 represents the maximum of this pressure peak P_{max} and the pressure at the end of the pulse duration, P_{Tpul} , obtained analytically as a function of the intensity, together with the maximum pressure P_{max} calculated from the experimental FSV using formula (1). The pulse duration does not affect the maximum pressure, however, longer pulses induce lower pressures at time T_{pul} . In the entire range studied, the maximum pressures calculated from the experimental FSVs are in between the fits of the maximum pressure and the pressure at T_{pul} . It is therefore important to take the entire temporal pressure profile into account when using it as an input to simulate the target’s behavior under laser shock.

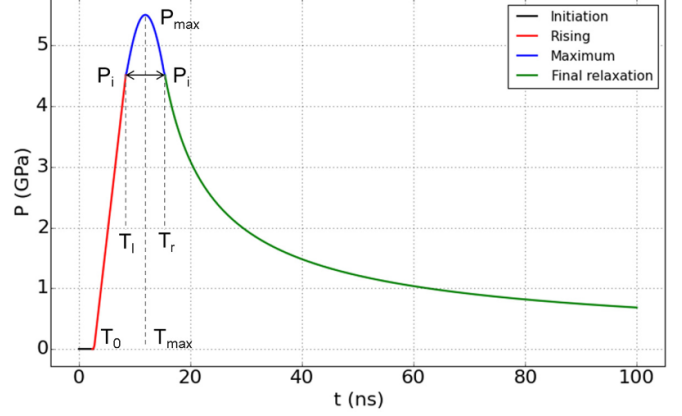


Figure 15. Analytic temporal pressure profile corresponding to a 7 ns FWHM Gaussian pulse at 532 nm with an incident laser intensity of 5 GW cm^{-2} under the WCR.

4.2. Water-confined regime

4.2.1. 532 nm. With the 7 ns Gaussian-shaped laser pulse, the pressure profile is also a Gaussian until the final release. For the purposes of this study, the profile was divided into four temporal zones, the initiation, the rise, the maximum, and the relaxation (figure 15). For each zone, an analytic formula has been fitted in order to reproduce the simulation over the entire area of validity. The intensities were set between 1 and 10 GW cm^{-2} for 7 to 20 ns FWHM Gaussian pulses. It should be noted that only the 7 ns simulations can be compared with experiments.

T_0 is defined as the time needed for the initiation of the ablation phenomena. For a Gaussian pulse, the intensity increase is slow, since the energy deposited needs some time to ablate the surface and create a plasma which will absorb the laser energy. The initial reflectivity of the aluminum surface, which controls T_0 , is set to 0.5. Once the aluminum is sufficiently ablated, the pressure rises drastically until it reaches its maximal value, P_{max} . After this maximum is reached at T_{max} , the medium slowly relaxes. The following equations describe the analytic formulation which enables the reproduction of the profile pressure using only the pulse duration T_{pul} and the maximum intensity, I , for Gaussian pulses.

- Initiation $t \leq T_0 : P(t) = 0$ with $T_0 = \frac{0.8 + 0.87 T_{\text{pul}}}{p^{0.35}}$
- Linear rise $t \leq T_l : P(t) = P_i \left(\frac{t - T_0}{T_l - T_0} \right)$ with $T_l = T_{\text{max}} - \frac{1}{2} T_{\text{pul}}$ and $P_i = 0.82 P_{\text{max}}$
- Maximal pressure $T_l \leq t \leq T_r : P(t) = P_{\text{max}} e^{-\left(\frac{t - T_{\text{max}}}{1.17 T_{\text{pul}}} \right)^2}$ with $T_r = T_{\text{max}} + \frac{1}{2} T_{\text{pul}}$
- Final release zone $t \geq T_r : P(t) = P_i \left(\frac{T_r - T_r \delta}{t - T_r \delta} \right)^n$.

The maximal pressure peak is reached at T_{max} , with $T_{\text{max}} = 1.7 T_{\text{pul}} (I - (1.3 - 0.13 T_{\text{pul}}))^{0.012}$, the highest values being achieved with $P_{\text{max}} = 2.2 I^{0.57}$. The coefficients n and δ , required for the calculation of the final relaxation are defined by equation (A12) in appendix A.2.

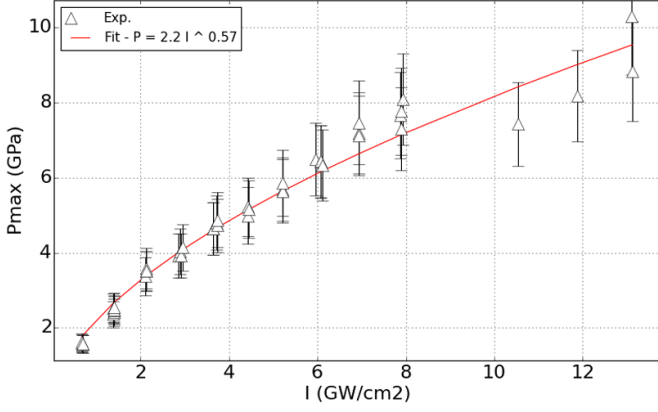


Figure 16. Maximum pressures calculated by analytic fits and formula (1) for 7 ns Gaussian pulses at 532 nm in the WCR.

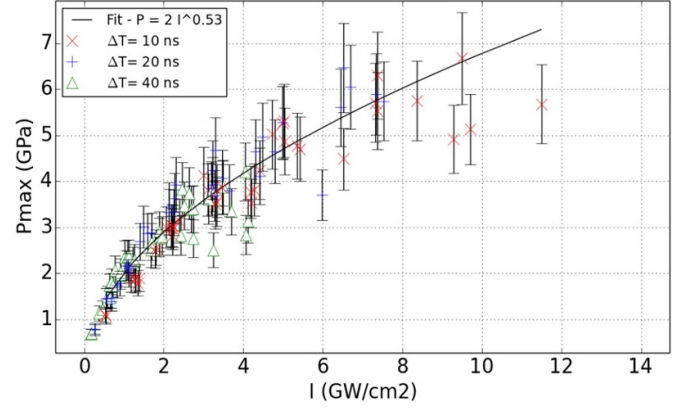


Figure 18. Maximum pressures calculated according to analytic fits and formula (1) for 10, 20 and 40 ns top-hat pulses at 1053 nm in the WCR.

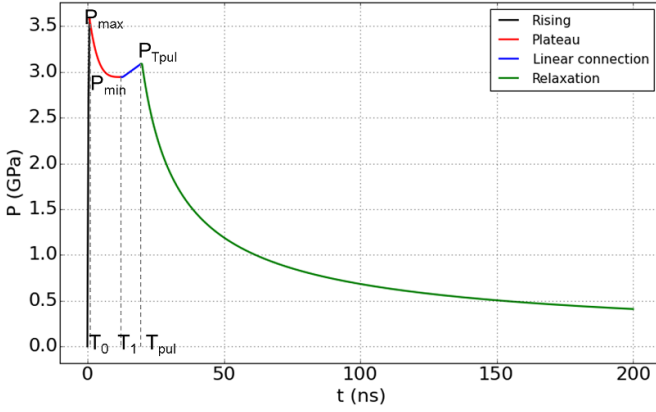


Figure 17. Analytic temporal pressure profile corresponding to a 20 ns top-hat pulse at 1053 nm with an incident laser intensity of 3 GW cm⁻² under the WCR.

It can be seen from these formulas that the maximum of the pressure does not depend on the pulse duration for a Gaussian pulse (this might not be true for other pulse shapes). The pulse duration has an influence on the pressure duration, which is to make its temporal shape longer. The maximum pressures calculated from the experimental FSVs presented in 7 using formula (1) [26] were plotted together with the maximum values of P_{\max} calculated via the fit in figure 16. These two methods of maximum pressure determination are in very good agreement until the water breakdown phenomenon occurs.

4.2.2. 1053 nm. For water-confined regimes at 1053 nm, the temporal pressure profiles obtained from the simulation with intensities ranging from 1 to 6 GW cm⁻² and top-hat pulses from 10 to 40 ns were separated into four zones (figure 17). The analytic equations of the pressure profile dependence on the laser intensity, I (GW cm⁻²) and the pulse duration T_{pul} [ns] are as follows:

- Quadratic rising $t \leq T_0 : P(t) = P_{\max} \left(1 - \left(1 - \frac{t}{T_0} \right)^2 \right)$
with $T_0 = \frac{2.4}{I}$ and $P_{\max} = 2I^{0.53}$

- Plateau $T_0 \leq t \leq \min(T_1, T_{\text{pul}}) : P(t) = P_{\min} + (P_{\max} - P_{\min}) \left(\frac{T_1 - t}{T_1 - T_0} \right)^4$
with $T_1 = \max(12, 16 - I)$ and $P_{\min} = 1.79 I^{0.453}$
- Linear connection $T_1 \leq t \leq \min(T_{\text{pul}}) : P(t) = \frac{P_{40\text{ns}} - P_{\min}}{40 - T_1} (t - T_1) + P_{\min}$ with $P_{40\text{ns}} = 1.97I^{0.53}$
- Final releasing zone $t \geq T_{\text{pul}} : P(t) = P(T_{\text{pul}}) \left(\frac{1 - \delta}{t/T_{\text{pul}} - \delta} \right)^n$
with $n = 0.68 + 0.5e^{-(0.1T_{\text{pul}} - 0.5)I}$ and $\delta = 0.52$
 $\left(1 - e^{-(0.011T_{\text{pul}}^{1.56})I} \right)$.

The pressure temporal profiles are not Gaussian shapes, however the maximum pressure P_{\max} is close to the pressure at the end of the laser pulse, P_{pul} . The maximal pressures P_{\max} calculated from the fit are plotted as a function of the incident intensities together with the P_{\max} calculated by equation (1) from the experimental FSVs. Similarly to the WCR at 532 nm, the two methods of P_{\max} determination are in good agreement. The pulse duration ΔT has no influence on P_{\max} , however, a longer pulse duration induces a longer pressure, therefore it is important to take into account the entire temporal profile of the pressure given by the above equations.

5. Conclusions

In this paper, we presented the experimental FSVs of pure aluminum, as measured by VISAR in three different laser labs. This work synthesizes a significant range of input parameters covering two irradiation regimes (direct and water confined), three wavelengths (from 532 to 1053 nm), two laser pulse shapes (Gaussian and top-hat), four laser-pulse durations (from 7 to 40 ns) and five focal-spot sizes (from 1 to 5 mm) with round and square shapes. Although the experiments were conducted with several laser configurations, the results collected demonstrated good consistency. More precisely, it was shown that with similar wavelengths and pulse durations, the shape of the focal spot does not have an effect on the maximal FSV. Due to the good agreement of the simulation results with the experimental data, the reliability of the ESTHER code was extended to a broader range of validity, making it now possible to obtain physical data characterizing

Table 2. Plasma characterization of water-confined laser shock at $\lambda = 532, 1029$ and 1053 nm, $\Delta T = 7, 10, 20,$ and 40 ns for pure aluminum, thickness = $500 \mu\text{m}$.

Laser parameter	$\lambda = 523$ nm	$\lambda = 1029$	$\lambda = 1053$	$\lambda = 1053$	$\lambda = 1053$
	$-\Delta T = 7$ ns	nm— $\Delta T = 10$ ns	nm— $\Delta T = 10$ ns	nm— $\Delta T = 20$ ns	nm— $\Delta T = 40$ ns
Breakdown threshold (GW cm ⁻²)	8–10	5–6	5–6	3–4	2–3
Breakdown threshold (J/cm ⁻²)	56–70	50–60	50–60	60–80	80–120
Ablation pressure at the threshold (GPa)	7.2–8.2	4.7–5.2	4.7–5.2	3.6–4.2	2.9–3.6
Range of simulated intensities (GW cm ⁻²)	2.5–6.0	//	1.3–5.0	1.5–2.3	0.8–2.0
Plasma temperature range (eV)	10–14	//	8–12	10–12	8–13
Range of plasma thickness (μm)	8–12	//	9–13	17–20	20–30
Range of ablated aluminum thickness (μm)	1.7–3.0	//	2.2–2.3	3.5–3.9	3.2–5.5

the plasma produced (table 2). We have presented analytic fits of the temporal pressure profiles that can be used in any mechanical simulation software to simulate the behavior of aluminum targets under laser shock. In a future investigation, the influence of changing the pulse duration and spatial shape at 532 nm will be investigated.

Appendix A. Parameters for temporal pressure profile scaling law

A.1. Direct illumination regime

The parameters P_{\max} , P_i (pressure at time equals T_i), p , n and δ (figure 13) were adjusted for the entire intensity and pulse duration range. The results are given below, with I and T_{pul} in ns and GW cm⁻², respectively.

$$P_{\max} = 0.56 + 0.08 I - 3.2 \times 10^{-4} I^2 \text{ for } I \leq 100 \quad (\text{A1})$$

$$P_{\max} = 2.52 + 0.0238 I \text{ for } I \geq 100 \quad (\text{A2})$$

$$P_m = 0.092 I^{0.623} \text{ for } I \leq 100 \quad (\text{A3})$$

$$P_m = 0.162 + 0.0166 I \text{ for } I \geq 100 \quad (\text{A4})$$

$$p = \frac{\ln\left(\frac{P_{\max}}{P_m}\right)}{\ln\left(\frac{40}{T_0}\right)}. \quad (\text{A5})$$

The parameters P_{\max} and p do not depend on the pulse duration, therefore they were adjusted for the longest pulse duration, i.e 40 ns. The minimal pressure, P_m , corresponds to the pressure obtained at the end of this pulse duration. The other three parameters related to the relaxation, P_i , n , and δ

are given by the following equations. They depend on the pulse duration T_{pul} .

$$P_i = 0.11 + 0.011 I^* \text{ for } I^* \leq 240 - 3.4 T_{\text{pul}} \quad (\text{A6})$$

$$P_i = (2.79 - 0.09 T_{\text{pul}} + 1.12 \times 10^{-3} T_{\text{pul}}^2) + 2 \times 10^{-3} I^* \text{ for } I^* \geq 240 - 3.4 T_{\text{pul}} \quad (\text{A7})$$

$$I^* = (1.1 - 9.76 \times 10^{-3} T_{\text{pul}}) I \quad (\text{A8})$$

$$n = (0.5 + 1.76 \times 10^{-2} T_{\text{pul}}) e^{-\left(\frac{I^{**} - 115}{100}\right)^2} + 1.14 - 1.06 \times 10^{-2} T_{\text{pul}} + 1.37 \times 10^{-4} T_{\text{pul}}^2 \quad (\text{A9})$$

$$\delta = 0.83 - (0.467 - 2.45 \times 10^{-3} T_{\text{pul}} + 1.75 \times 10^{-4} T_{\text{pul}}^2) e^{-\left(\frac{I^{**} - 100}{100}\right)^2} \quad (\text{A10})$$

$$I^{**} = (0.84 + 0.016 T_{\text{pul}}) I. \quad (\text{A11})$$

A.2. WCR at 532 nm, figure 15

$$n = \max\left(0.72; 0.72 \left(\frac{I_s}{I}\right)^{0.25}\right) \quad (\text{A12})$$

$$\delta = \min\left(0.57; 0.57 + (0.16 - 2.3 \times 10^{-2} T_{\text{pul}} + 1.4 \times 10^{-3} T_{\text{pul}}^2) (I - I_s)\right) I_s = 5.4 - 0.22 T_{\text{pul}}.$$

ORCID iDs

Marine Scius-Bertrand  <https://orcid.org/0000-0002-2695-9557>

Laurent Berthe  <https://orcid.org/0000-0002-9978-9843>

References

- [1] Antoun T, Seaman L, Curran D R, Kanel G I, Razorenov S V and Utkin A V 2003 *Spall Fracture* (New York: Springer)
- [2] Meyers M A 1994 *Dynamic Behavior of Materials* (New York: Wiley)
- [3] Clauer A H 2019 Laser shock peening, the path to production *Metals* **9** 626
- [4] Yuan J and Gupta V 1993 Measurement of interface strength by the modified laser spallation technique. i. experiment and simulation of the spallation process *J. Appl. Phys.* **74** 2388–96
- [5] Bolis C, Berthe L, Boustie M, Arrigoni M, Barradas S and Jeandin M 2007 Physical approach to adhesion testing using laser-driven shock waves *J. Phys. D: Appl. Phys.* **40** 3155–63
- [6] Ballard P, Fournier J, Fabbro R and Frelat J 1991 Residual stresses induced by laser-shocks *J. Phys. IV (Proc.)* **01** C3-487–94
- [7] Fairand B P, Wilcox B A, Gallagher W J and Williams D N 1972 Laser shock-induced microstructural and mechanical property changes in 7075 aluminum *J. Appl. Phys.* **43** 3893–5
- [8] Peyre P, Fabbro R, Berthe L and Dubouchet C 1996 Laser shock processing of materials, physical processes involved and examples of applications *J. Laser Appl.* **8** 135–41
- [9] Peyre P, Fabbro R, Merrien P and Lieurade H P 1996 Laser shock processing of aluminium alloys. Application to high cycle fatigue behaviour *Mater. Sci. Eng. A* **210** 102–13
- [10] Clauer A H 1996 Laser shock peening for fatigue resistance **217** 230
- [11] Vossen J L 1978 Measurements of film-substrate bond strength by laser spallation *Adhesion Measurement of Thin Films, Thick Films and Bulk Coatings* (Conshohocken, PA: ASTM International) pp 122–33
- [12] Berthe L, Arrigoni M, Boustie M, Cuq-Lelandais J P, Broussillou C, Fabre G, Jeandin M, Guipont V and Nivard M 2011 State-of-the-art laser adhesion test (LASAT) *Nondestruct. Test. Eval.* **26** 303–17
- [13] Bardy S, Aubert B, Berthe L, Combis P, Hébert D, Lescoute E, Rullier J-L and Videau L 2016 Numerical study of laser ablation on aluminum for shock-wave applications: development of a suitable model by comparison with recent experiments *Opt. Eng., Bellingham* **56** 011014
- [14] Sagnard M, Ecault R, Touchard F, Boustie M and Berthe L 2019 Development of the symmetrical laser shock test for weak bond inspection *Opt. Laser Technol.* **111** 644–52
- [15] Ecault R, Dominguez N and Voillaume H 2020 Laser Shock Adhesion test for composite bonding assessment *Compos. Struct.* **247** 112441
- [16] Mora P 1982 Theoretical model of absorption of laser light by a plasma *Phys. Fluids* **25** 1051–6
- [17] Ambartsumyan R, Basov N, Bočko V, Zuev V, Krokhin O, Kryukov P, Senat-Skič Y and Stočlov Y 1965 Heating of matter by focused laser radiation *Sov. J. Exp. Theor. Phys.* **21** 1061–4
- [18] Anderholm N C 1970 Laser-generated stress waves *Appl. Phys. Lett.* **16** 113–15
- [19] O'Keefe J D and Skeen C H 1972 Laser-induced stress-wave and impulse augmentation *Appl. Phys. Lett.* **21** 464–6
- [20] Peyre P and Fabbro R 1995 Laser shock processing: a review of the physics and applications *Opt. Quantum Electron.* **27** 1213–29
- [21] Fabbro R, Fournier J, Ballard P, Devaux D and Virmont J 1990 Physical study of laser-produced plasma in confined geometry *J. Appl. Phys.* **68** 775–84
- [22] Berthe L, Fabbro R, Peyre P, Tollier L and Bartnicki E 1997 Shock waves from a water-confined laser-generated plasma *J. Appl. Phys.* **82** 2826–32
- [23] Berthe L, Fabbro R, Peyre P and Bartnicki E 1998 Experimental study of the transmission of breakdown plasma generated during laser shock processing *EPJ Appl. Phys.* **3** 215–18
- [24] Sollier A, Berthe L and Fabbro R 2001 Numerical modeling of the transmission of breakdown plasma generated in water during laser shock processing *EPJ Appl. Phys.* **16** 131–9
- [25] Le Bras C *et al* 2019 Laser shock peening: toward the use of pliable solid polymers for confinement *Metals* **9** 1–13
- [26] Tollier L, Fabbro R and Bartnicki E 1998 Study of the laser-driven spallation process by the velocity interferometer system for any reflector interferometry technique. I. Laser-shock characterization *J. Appl. Phys.* **83** 1224–30
- [27] Sano Y, Mukai N, Okazaki K and Obata M 1997 Residual stress improvement in metal surface by underwater laser irradiation *Nucl. Instrum. Methods Phys. Res. B* **121** 432–6 Materials Synthesis and Modification by Ion and/or Laser Beams
- [28] Barker L M and Hollenbach R E 1972 Laser interferometer for measuring high velocities of any reflecting surface *J. Appl. Phys.* **43** 4669–75
- [29] Barker L M and Schuler K W 1974 Correction to the velocity-per-fringe relationship for the VISAR interferometer *J. Appl. Phys.* **45** 3692–3
- [30] Tollier L and Fabbro R 1998 Study of the laser-driven spallation process by the VISAR interferometry technique. II. Experiment and simulation of the spallation process *J. Appl. Phys.* **83** 1231–7
- [31] Divoky M *et al* 2020 Performance comparison of yb:rag ceramics and crystal gain material in a large-area, high-energy, high average-power diode-pumped laser *Opt. Express* **28** 3636–46
- [32] CUQ-LELANDAIS J-P 2010 Etude du comportement dynamique de matériaux sous choc laser sub-picoseconde *PhD Thesis Ecole Nationale Supérieure de Mécanique et d'Aérotechnique, Poitiers* (<http://www.theses.fr/2010ESMA0017>)
- [33] Boustie M, Cuq-Lelandais J P, Bolis C, Berthe L, Barradas S, Arrigoni M, de Resseguier T and Jeandin M 2007 Study of damage phenomena induced by edge effects into materials under laser driven shocks *J. Phys. D: Appl. Phys.* **40** 7103–8
- [34] Steinberg D J, Cochran S G and Guinan M W 1980 A constitutive model for metals applicable at high-strain rate *J. Appl. Phys.* **51** 1498–504
- [35] Bardy S, Aubert B, Bergara T, Berthe L, Combis P, Hébert D, Lescoute E, Rouchausse Y and Videau L 2020 Development of a numerical code for laser-induced shock waves applications *Opt. Laser Technol.* **124** 105983
- [36] Colombier J P, Combis P, Bonneau F, Le Harzic R and Audouard E 2005 Hydrodynamic simulations of metal ablation by femtosecond laser irradiation *Phys. Rev. B—Condens. Matter Mater. Phys.* **71** 1–6
- [37] Cuq-Lelandais J P, Boustie M, Berthe L, De Rességuier T, Combis P, Colombier J P, Nivard M and Claverie A 2009 Spallation generated by femtosecond laser driven shocks in thin metallic targets *J. Phys. D: Appl. Phys.* **42** 065402
- [38] Palik E D 1998 *Handbook of Optical Constants of Solids* (New York: Academic) vol 3
- [39] Spitzer L 2006 *Physics of Fully Ionized Gases* (New York: Dover Publications)

- [40] Kedenburg S, Vieweg M, Gissibl T and Giessen H 2012 Linear refractive index and absorption measurements of nonlinear optical liquids in the visible and near-infrared spectral region *Opt. Mater. Express* **2** 1588–1611
- [41] Clauer A H, Fairand B P and Wilcox B A 1977 Laser shock hardening of weld zones in aluminum alloys *Metallurgical Trans. A* **8** 1871–6
- [42] Montross C S, Wei T, Lin Y, Clark G and Mai Y-W 2002 Laser shock processing and its effects on microstructure and properties of metal alloys: a review *Int. J. Fatigue* **24** 1021–36